Nuclear Materials and Energy 41 (2024) 101786

Contents lists available at ScienceDirect

Nuclear Materials and Energy

journal homepage: www.elsevier.com/locate/nme

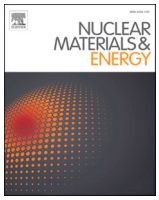

# Experimental insights on iron-based alloys corrosion in water cooled loops

Martina Molinari [a,*], Eugenio Lo Piccolo [b], Raffaele Torella [b], Matteo D'Onorio [a], Nicholas Terranova [c], Gianfranco Caruso [a]

[a] Department of Astronautical, Electrical and Energy Engineering (DIAEE) – Nuclear Section, Sapienza University of Rome, Corso Vittorio Emanuele II 244, 00186 Rome, Italy
[b] RINA Consulting – Centro Sviluppo Materiali S.p.A. Roma, Via di Castel Romano 100, 00128 Rome, Italy
[c] ENEA Fusion and Technology for Nuclear Safety and Security Department, Frascati RC, Via Enrico Fermi 45, 00044 Frascati, Italy

ARTICLE INFO

*Keywords:*
Potassium hydroxide
Oxygen control
Corrosion
Corrosion tests
EUROFER
High-temperature high-pressure

ABSTRACT

This paper presents experimental findings on the behavior of iron-based alloys in environmental conditions typical of nuclear fusion technology, specifically focusing on material degradation, which is a critical aspect for the water cooling system of EU DEMO breeding blankets. The experimental campaign investigates potassium hydroxide's role as an alkalizing agent, testing various concentrations to assess its impact on corrosion resistance. Additionally, it examines how oxygen levels affect localized corrosion development, which is crucial for mitigating corrosion risks in fusion applications. Seven 1000-hour tests were conducted to determine optimal conditions for corrosion reduction. Findings include identifying an oxygen concentration threshold to prevent piping cracking on EUROFER97 specimens.

## Introduction

The cooling circuit operation in a nuclear Fusion Power Plant (FPP) involves complex and consequential phenomena, among which the variation in corrosion rates is particularly critical. More than just a technical issue, these variations significantly affect the degradation of materials in the circuit, jeopardizing the plant structural integrity, with relevant safety consequences. Moreover, in the unique and harsh environment of a FPP, the burning plasma's neutron field activates both the structural materials and their Corrosion Products (CPs). Once activated, these CPs evolve from a simple byproduct of corrosion into a potential radiological hazard, emitting radiation that poses a risk to the plant personnel and environment.

The literature on nuclear safety and radiological protection has extensively documented that Activated CPs (ACPs) are a significant radiological source term for occupational dose assessment. Once mobilized, ACP can pose a substantial risk during accidental scenarios [1–4]. Therefore, understanding the corrosion process, managing its byproducts, and mitigating its effects are essential for the safe and efficient operation of FPPs.

As detailed in [5], corrosion is not a monolithic process; there are various types of corrosion. The most common classification is between wet and dry corrosion. Wet corrosion is the prevalent type of corrosion in the context of a cooling circuit, because the primary catalyst for corrosion phenomena is water, which acts as the coolant in the system.

This prevalence underscores the importance of water chemistry in managing and mitigating corrosion phenomena. Optimizing water chemistry, therefore, is not just a matter of efficiency; it is a fundamental strategy for ensuring the safety and longevity of the plant. The water chemistry of the cooling circuit within a FPP is a matter of balance. It necessitates the addition of an alkalizing agent to counteract acidification, which can result from radiolysis or increased temperatures. Furthermore, maintaining an inert atmosphere is essential to prevent the creation of an oxidizing environment or the solution's carbonation. The safety measures are not optional; they are vital for the safe operation of the plant. In addition to the formation of a high rate of corrosion products, localized corrosion phenomena could affect the structural integrity of the piping material; in this case, the damages could be initiating events for accidental scenarios.

In the frame of the Work Package Breeding Blanket (WP-BB) of the EUROFusion consortium, experimental analyses have been conducted to gather data on the corrosion behavior of different alloys under specific environmental conditions of the Water-Cooled Lithium Lead (WCLL) BB. The WCLL BB concept, under design for EU-DEMO, is operated in conditions typical of a PWR, with water temperature ranging from 295 °C to 328 °C and an operating pressure of 155 bars. These alloys include

* Corresponding author.
*E-mail address:* martina.molinari@uniroma1.it (M. Molinari).

https://doi.org/10.1016/j.nme.2024.101786
Received 2 August 2024; Received in revised form 10 October 2024; Accepted 21 October 2024
Available online 22 October 2024

EUROFER97 and Stainless Steel 316L, with Potassium Hydroxide (KOH) being used as the base. These studies are part of a broader effort to understand and manage corrosion in FPPs. For the performed experimental analyses, the KOH has been used as alkali rather than lithium hydroxide, because of the successfully primary coolant pH control in Water-Water Energetic Reactors (VVER) [6], and one of the goals of this work to obtain a better pH control performing high-temperature high-pressure tests.

This already mentioned approach aligns with the one in [7], where experimental activities were conducted to verify different water chemistry compositions for FPPs. However, Lithium Hydroxide (LiOH) and Ammonia (NH3) were used as the base in this case. While using different bases, these studies share a common goal: to provide valuable insights into the corrosion process and its management, contributing to the safe and efficient operation of FPPs.

This paper presents the results obtained from seven different expositions, focusing on the occurrence of localized corrosion. These findings contribute to the broader understanding of corrosion in FPPs, providing valuable insights for improving operational safety and efficiency. By examining these results, we can better understand the corrosion process, its causes, and its effects, leading to more effective strategies for managing corrosion and ensuring the safety and efficiency of FPPs. In addition, this paper aims to contribute to the ongoing studies on corrosion in FPPs. Providing a comprehensive analysis of the corrosion process and its implications will support the development of more effective strategies for managing this corrosion phenomenon and ensuring long-term safety.

## Case study: Corrosion of Fe-base alloys

Both EUROFER97 and SS316 are iron-based alloys [8–10], which implies that the CPs under study are mainly formed starting from the Fe corrosion.

Fe-based alloy corrosion is a process widely described in the literature for different environmental applications, whether nuclear fusion applications or not. There are examples in the literature where Fe-based alloy corrosion behavior has been studied in sulphuric acid environments [11] or supercritical water environments [12]. The problem of corrosion and CP movement and activation into the environment of a FPP affects not only fusion applications, like in [13] where the effect of lithium breeders on EUROFER97 corrosion is described, but also fission applications.

As explained in [14], the corrosion chemical reactions give different products according to the metal considered. In the case of Fe, the overall reaction is given by:

$$3Fe + 4H_2O \rightarrow Fe_3O_4 + 4H_2$$

Where $Fe_3O_4$ is a compound called magnetite and is composed of Fe with two oxidation numbers, in particular, $Fe^{+2}$ and $Fe^{+3}$. For this reason, the magnetite formulation can also be written as $FeO(Fe_2O_3)$.

The materials employed in this experimental campaign consist of flat hot rolled coupons fabricated from EUROFER97 and SS316L, all meticulously crafted within the laboratory. Each specimen adheres to standardized dimensions of 20x20x3 mm. The chemical composition of EUROFER97 specimens is synthetically outlined in Table 1, while the chemical composition of SS316L specimens is detailed in Table 2.

For the EUROFER97 specimens, the application of grease is foreseen, as it is not a stainless alloy, to pre-empt corrosion prior to exposure within the autoclave.

**Table 2**
SS316L chemical composition (wt %).

| Material | C | Mn | Cr | Ni | Ti | Mo | Si | Cu |
|---|---|---|---|---|---|---|---|---|
| SS316L | 0.01 | 1.0 | 16.63 | 10.1 | 0.007 | 2.06 | 0.32 | 0.37 |

## High-Pressure High-Temperature loop

The seven tests were performed in RINA-CSM laboratories, with a corrosion testing loop tailored explicitly for the experimental conditions required. This corrosion loop test apparatus, named High-Pressure High-Temperature (HPHT), comprises:

- an autoclave of 1.5 L,
- a heat exchanger,
- the pipeline and the pumping system,
- a pre-heater and a deaeration vessel

All of the components cited above are shown in Fig. 1.

The superalloy Ni-based autoclave is equipped with an electrical heater capable of reaching 300 °C. The heat exchanger cools the solution from 300 °C to 25 °C to reach a temperature suitable for the piping system. The pumping system propels the solution with a velocity of 2 m/s, corresponding to a mass flow rate of 5.72 kg/s and a volumetric flow rate of 28.8 $m^3$/h. The fluid velocity has been maintained under the limit value of 7 m/s [15]. Downstream to the pumping system, a preheater heats up the solution to 100 °C before re-entering into the autoclave. The direction of the flow during the test phase is shown in Fig. 1 with a black arrow.

Prior to each experimental test, the HPHT loop underwent a rigorous leak test using flowing nitrogen at a pressure exceeding the experimental pressure requirement by 20 %. Nitrogen was selected due to its lower molecular weight compared to the solution. Therefore, the absence of nitrogen leaks from the seals and junctions ensures the integrity of the solution containment.

Furthermore, both the autoclave and the loop were thoroughly cleaned with flowing ultra-pure water before and after each experimental test to eliminate any presence of deposited particles that could potentially contaminate subsequent tests.

## Test Description

Each experimental test is divided into three different phases: the pretest phase, the test phase, and the post-test phase. All of them are described in the following.

### *Pretest phase*

In the preparatory phase, the entire experimental setup is arranged. The HPHT loop undergoes a cleaning process using flowing ultra-pure water heated up to 300 °C. Meanwhile, the laboratory chemistry department prepares the solution, measuring its pH before transferring it into the deaeration vessel within a short timeframe to prevent contamination and carbonation of the solution.

**Table 1**
EUROFER97 chemical composition (wt %).

| Material | Cr | Ni | Mn | Ti | V | Al | Ta | W | Mo |
|---|---|---|---|---|---|---|---|---|---|
| EUROFER97 | 8.89 | 0.01 | 0.51 | 0.005 | 0.34 | 0.01 | 0.10 | 0.92 | 0.01 |
| | **C** | **Si** | **P** | **Sn** | **Sb** | **N** | **S** | **Co** | **Nb** |
| | 0.11 | 0.05 | 0.005 | 0.001 | 0.001 | 0.21 | 0.003 | 0.06 | 0.01 |

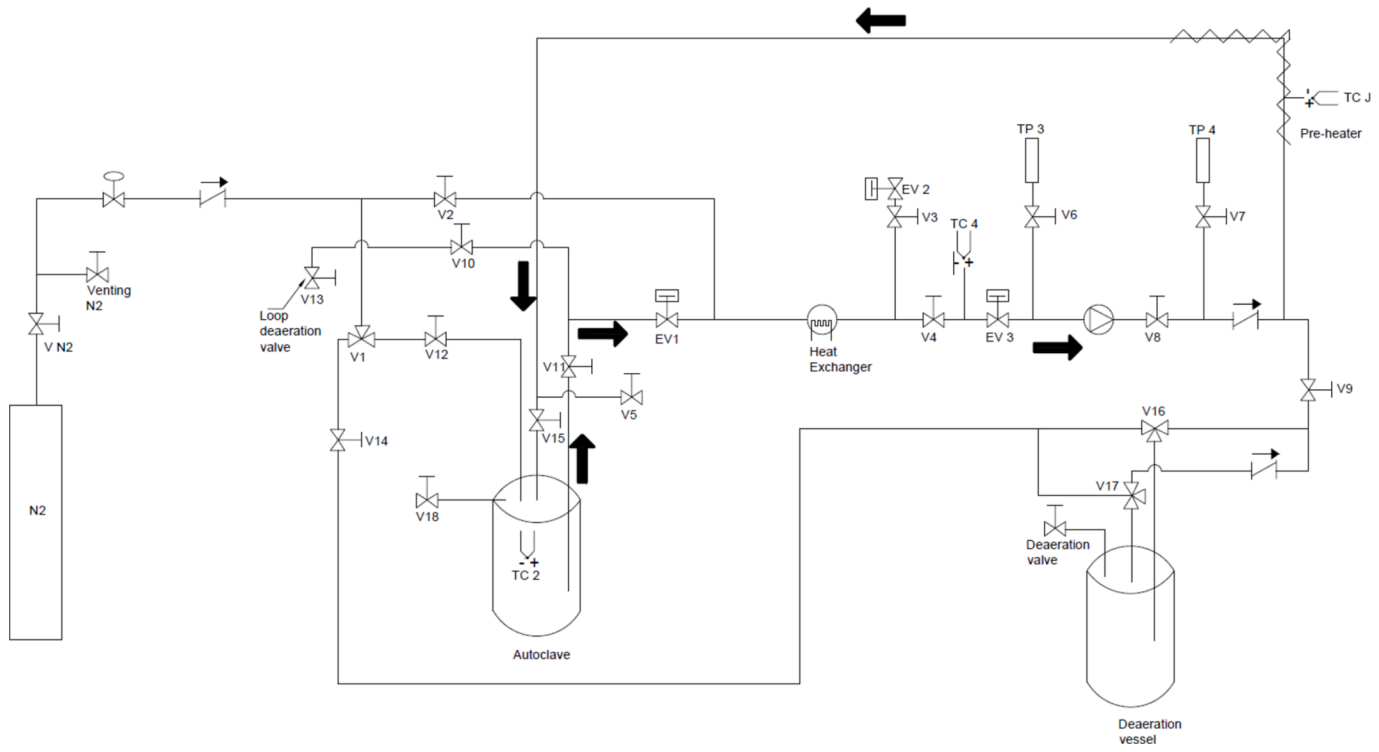


**Fig. 1.** HPHT schematic loop.

Furthermore, the solution container is exclusively designated for this corrosion test campaign, ensuring no contaminations from other chemical substances. Once the solution is in the deaeration vessel, it is sealed off, and nitrogen is bubbled through to maintain a controlled environment. The vessel remains isolated from the rest of the loop throughout this process.

A magnetic stirring is employed to prevent errors in oxygen measurement resulting from oxygen stratification within the solution. It has to be clarified that the oxygen measurement was performed only in the deaeration vessel before the solution was poured from the deaeration vessel to the vessel. An in-line oxygen measurement is not possible with the configuration shown in Fig. 1.

The specimens, previously produced by the dedicated department, are degreased with Acetone ($C_3H_6O$) and weighed before the test. All specimens are systematically identified using an alphanumeric code, as notable in Fig. 2. Subsequently, the specimens are carefully positioned within the autoclave, ensuring a sufficient distance between each specimen, as shown in Fig. 2.

Following the allocation of the specimens, the autoclave is securely closed and sealed. This closure process is facilitated by a system of pistons activated by compressed air, followed by the manual sealing of the autoclave head.

The concluding step of the pretest phase involves the complete deaeration of the entire loop. This is accomplished by flowing nitrogen, which displaces any pre-existing air from the loop into an air trap connected to the autoclave via a plastic tube equipped with a non-return valve.

*Test phase*

The campaign encompasses seven tests, with the primary specifications outlined in Table 3. From these tests, two distinct outcomes were derived. Initially, a more consistent pH pattern was noted throughout the test duration by altering the KOH concentration within the solution (shown in bold within the brackets – column "Solution"). Furthermore, starting from the third test, after achieving a relatively stable pH trajectory, the oxygen concentration within the solution was regulated (shown in bold within the brackets – column "$O_2$") to identify a

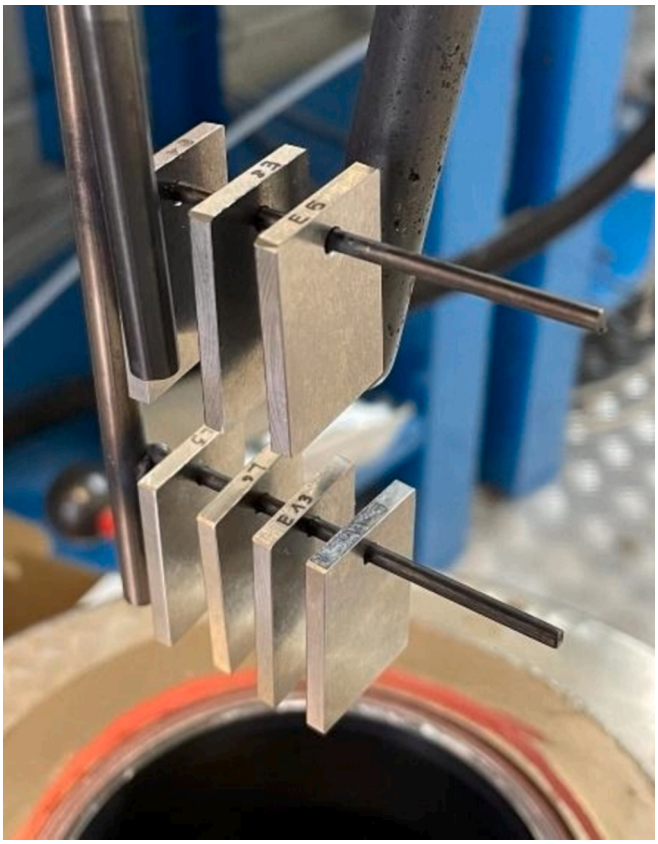

**Fig. 2.** Specimens allocated into the autoclave.

**Table 3**
Test conditions.

| Test N. | Solution | $O_2$ [ppb] | Specimen type | Pressure [bar] | Temperature [°C] | Time [h] | Aim |
|---|---|---|---|---|---|---|---|
| 1 | KOH **(5 ppm)** | < 10 | EUROFER SS316L | 100 | 300 | 1000 | Looking for pH stability |
| 2 | KOH **(26 ppm)** | < 10 | EUROFER SS316L | 100 | 300 | 1000 | |
| 3 | KOH **(52 ppm)** | < 10 | EUROFER SS316L | 100 | 300 | 1000 | |
| 4 | KOH (52 ppm) | **100** | EUROFER | 100 | 300 | 1000 | Looking for localized phenomena |
| 5 | KOH (52 ppm) | **200** | EUROFER SS316L | 100 | 300 | 1000 | |
| 6 | KOH (52 ppm) | **300** | EUROFER SS316L | 100 | 300 | 1000 | |
| 7 | KOH (52 ppm) | **400** | EUROFER SS316L | 100 | 300 | 1000 | |

threshold value beyond which localized corrosion phenomena might manifest.

The electrical heater is activated at the onset of the test phase to attain the requisite experimental conditions. Once the desired temperature is reached, the pumping system is initiated, signaling the beginning of the test.

Throughout this phase, in tests 1, test 2, and test 3, samples of the solution are extracted weekly to establish a time-dependent pH graph. The exact volume of the collected solution is reintroduced from the deaeration vessel.

After 1000 h, the electrical heater is deactivated, and the autoclave can be opened after cooling the hot side of the loop. At this juncture, the specimens are individually packaged and prepared for post-test analysis, while two solution samples are procured for chemical analysis and pH measurement.

There are slight variations with respect to the DEMO WCLL BB thermal–hydraulic condition, such as the operating pressure and temperature. About the fluid velocity, it has been maintained at 2 m/s to avoid erosion phenomena, but in any case, is respecting the requirement of being below 7 m/s.

*Post-test phase*

The post-test phase consists of several meticulous steps, according to ASTM G1 standards, to analyze both specimens and the water solution while also entailing the cleaning of the loop.

The HPHT loop undergoes a comprehensive draining and cleaning procedure. After draining, the autoclave is meticulously cleaned using Acetone and ultra-pure water to eliminate any precipitated particles that may have emanated from the specimens during the test.

The pH of the water solution is measured using a pH meter at 25 °C in an air-controlled environment. The second sample is also analyzed to ascertain the concentration of various chemical elements released into the solution.

The specimens undergo various analyses to assess their condition comprehensively. One EUROFER97 specimen is designated for metallography analysis, while the remaining specimens undergo weighing and macroscopic and microscopic evaluations using an optical microscope. Subsequently, a pickling solution containing water, hydrogen chloride (HCl), and hexamethylenetetramine (HMTA) is applied to remove the oxide scale. Following the pickling treatment, the specimens are weighed again to determine corrosion rates via weight loss and undergo a second round of macroscopic and microscopic evaluation.

The metallography analysis for EUROFER97 specimens is conducted separately. These specimens are embedded in an Araldite resin matrix for oxide scale characterization using Scanning Electron Microscopy (SEM) and Energy Dispersive X-ray Spectroscopy (EDS or EDX). Specifically, SEM analysis is utilized to observe the oxide scale both on the surface and in cross-section and measure oxide scale thickness. In contrast, EDS analysis focuses on oxide scale composition characterization. Additionally, if localized corrosion is detected, specimens are examined using a 3D digital microscope to assess the depth and profile of each pit.

## Results: Chemical analysis

Multiple findings can be derived from the chemical analysis. Fig. 3 depicts the pH trend observed across test 1, test 2, and test 3. The graph illustrates the attainment of the objective by test 3, as evidenced by a more consistent pH trend. Subsequent to test 3, the concentration of KOH was maintained, as detailed in Table 3, and the focus shifted toward identifying localized corrosion phenomena.

Moreover, the other analysis gave the concentration of several chemical species released in water. These concentrations are summarized in Table 4.

## Results: Corrosion analysis

From a corrosion standpoint, as previously mentioned, corrosion rates were assessed by measuring the weight loss of the specimens. The

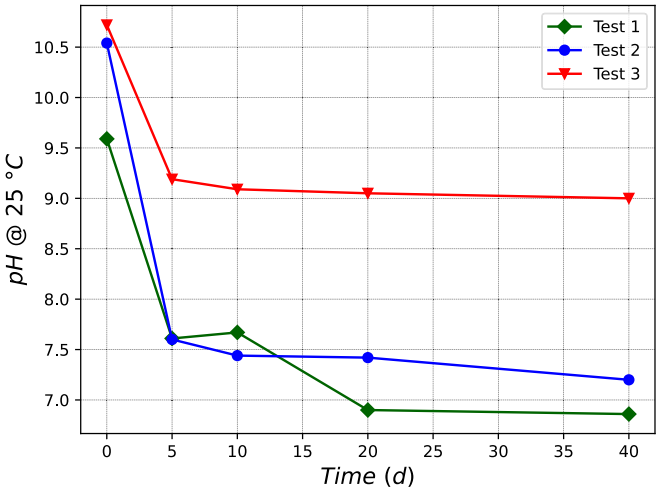


**Fig. 3.** Ph trend from test 1, test 2 and test 3.

**Table 4**
Releases concentration.

| Test N. | Fe [ppb] | Cr [ppb] | Ni [ppb] | Co [ppb] | Mo [ppb] | Cu [ppb] | W [ppb] | $pH_{in}$ T = 25 °C | $pH_{fin}$ T = 25 °C |
|---|---|---|---|---|---|---|---|---|---|
| 1 | 36 | 0.3 | 5 | 0.01 | 38 | 6 | 0.01 | 9.59 | 6.86 |
| 2 | 42 | 3 | 41 | 0.01 | 315 | 0.5 | 5 | 10.54 | 7.20 |
| 3 | 113 | 15.5 | 21.2 | 0.36 | 246 | 5.3 | 18.0 | 10.72 | 9 |
| 4 | 68 | 3.6 | 14.4 | 0.1 | 296 | 1.91 | 7.71 | 10.82 | 9.32 |
| 5 | 50.0 | 1.43 | 1.63 | 0.05 | 144.4 | 6.72 | 11.64 | 10.91 | 9.33 |
| 6 | 20.0 | 2.68 | 6.26 | 0.05 | 180.2 | 5.12 | 14.85 | 10.62 | 9.48 |
| 7 | 20.0 | 3.71 | 5.18 | 0.06 | 206.0 | 1.61 | 4.81 | 10.65 | 9.40 |

**Table 5**
Corrosion rates.

| Test N. | Material | Corrosion Rate w/o pickling treatment [μm/y] | Corrosion rate with pickling treatment (HCl + HMTA) [μm/y] |
|---|---|---|---|
| 1 | EUROFER97 | 3.0 ÷ 3.2 | 7.6 |
| | SS316L | 0.1 ÷ 0.2 | 1 |
| 2 | EUROFER97 | 1.9 ÷ 2.6 | 5.1 |
| | SS316L | 0.3 ÷ 0.4 | 1 |
| 3 | EUROFER97 | 0.0992 ÷ 0.1045 | 0.2325 ÷ 0.2625 |
| 4 | EUROFER97 | 0.0058 ÷ 0.069 | 0.0464 ÷ 0.1598 |
| | SS316L | 0.0086 ÷ 0.0201 | 0.023 |
| 5 | EUROFER97 | 0.1336 ÷ 0.1689 | 0.2497 ÷ 0.3081 |
| | SS316L | 0.0057 ÷ 0.0171 | 0.0228 ÷ 0.0229 |
| 6 | EUROFER97 | 0.0148 ÷ 0.1035 | 0.0148 ÷ 0.1568 |
| | SS316L | 0.0059 ÷ 0.0266 | 0.0059 ÷ 0.0266 |
| 7 | EUROFER | 0.1000 ÷ 0.4000 | 5.1 ÷ 7.9 |
| | SS316L | 0.1000 ÷ 0.4000 | 0.7000 |

corrosion rate evaluation is documented in Table 5. Notably, the corrosion rate post-pickling treatment exceeds that observed prior to treatment. This suggests that the formation of a magnetite layer occurs, serving as a protective barrier for the EUROFER alloy. The data presented in Table 5 are affected by an error related to the weight loss measurement. Specifically, this error is ± 1.67E-05 for EUROFER97 and ± 1.645E-05 for SS316L.

Of particular interest is test 6, which displayed a significantly smaller variation in corrosion rate compared to other tests. This could be attributed to one of two factors: either the absence of oxides prevented effective pickling, leaving the base metal vulnerable, or the pickling process was not sufficiently prolonged.

Furthermore, test 7 exhibited a higher corrosion rate, attributable to localized corrosion during the experiment's time span.

Following the assessment of corrosion rates, the oxide scale underwent characterization via SEM and EDS analysis. The SEM results are presented in both sectional and surface views, particularly utilizing Backscattered Electron Images (BEC or BEI) and Secondary Electron Images (SEI). BEC provides a morphological depiction, with brightness correlating to material density, while SEI offers topographical images [17]. Figs. 4–13 display the EUROFER97 oxide scale with sectional and surface views of the specimens, respectively, with associated chemical conditions of the solutions.

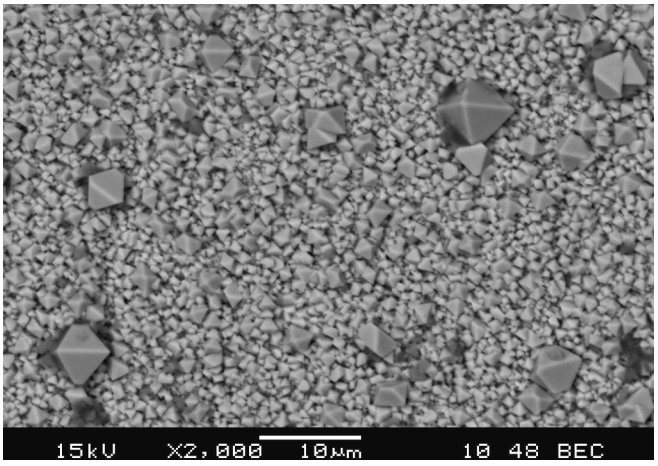


**Fig. 5.** Test 3 in surface view.

During the EDS analysis, the adherent corrosion layer thickness has been measured. Findings are reported in Table 6.

Table 6 presents information related to the thickness of the oxide. The compositions of the oxide layers are delineated in Table 8 and Table 9, detailing both the layer adherent to the base metal and the layer above, which is not adherent to the base metal.

Upon comparison of Table 8 and Table 9, it is observed that for test 3, there exists a nearly identical composition. This occurrence may be

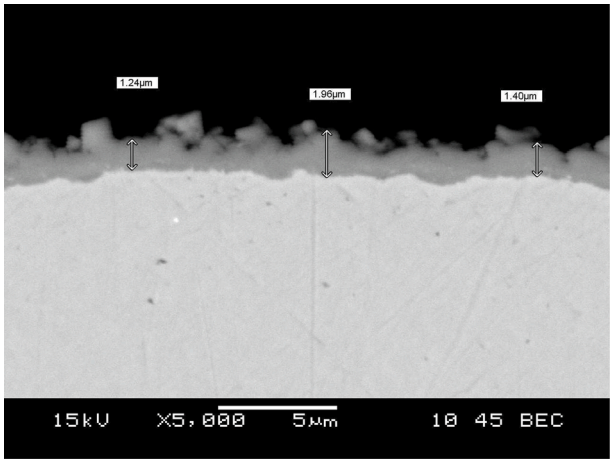


**Fig. 4.** Test 3 in section view.

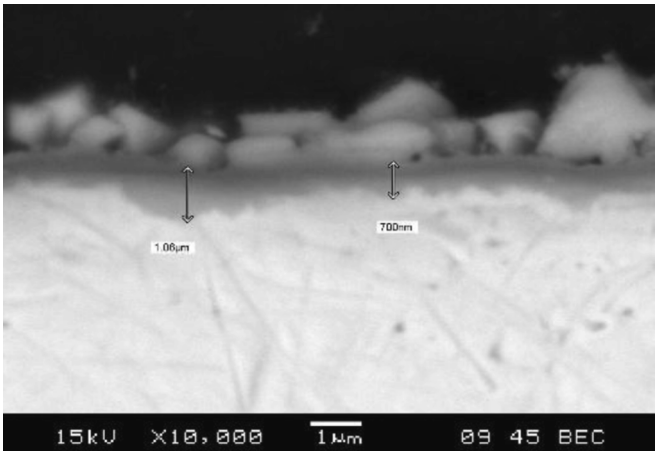


**Fig. 6.** Test 4 in section view.

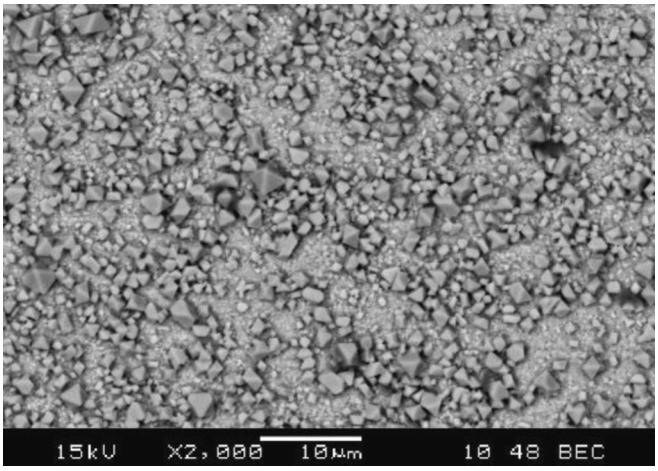


**Fig. 7.** Test 4 in surface view.

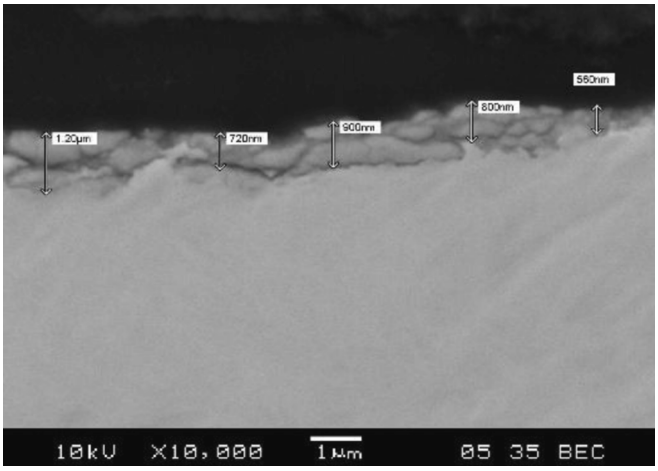


**Fig. 8.** Test 5 in section view.

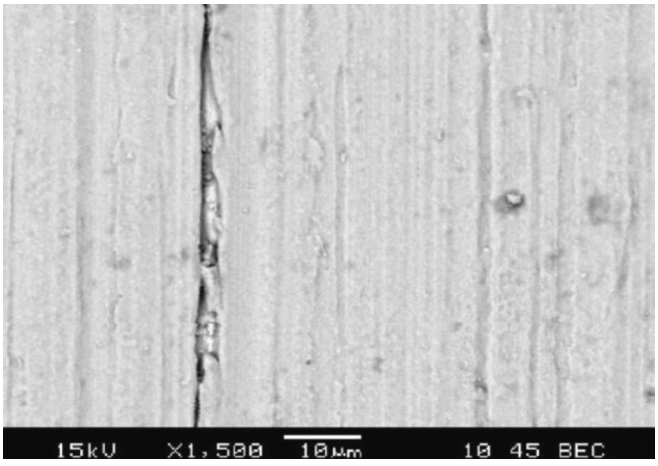


**Fig. 9.** Test 5 in surface view.

attributed to the predominant presence of the non-adhesive corrosion layer, posing challenges in pinpointing a distinct area within the adherent corrosion layer during SEM analysis.

Localized corrosion phenomena were absent in the post-test analysis until test 6. However, in test 7, two pits were identified on separate EUROFER97 specimens. A 3D digital analysis was conducted on these specimens to ascertain the characteristic dimensions of each pit.

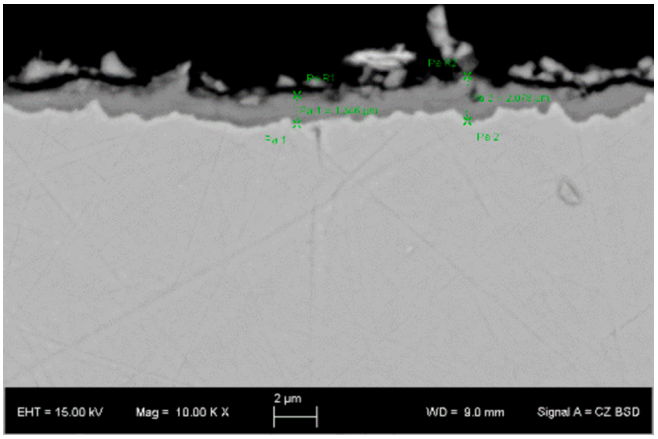


**Fig. 10.** Test 6 in section view.

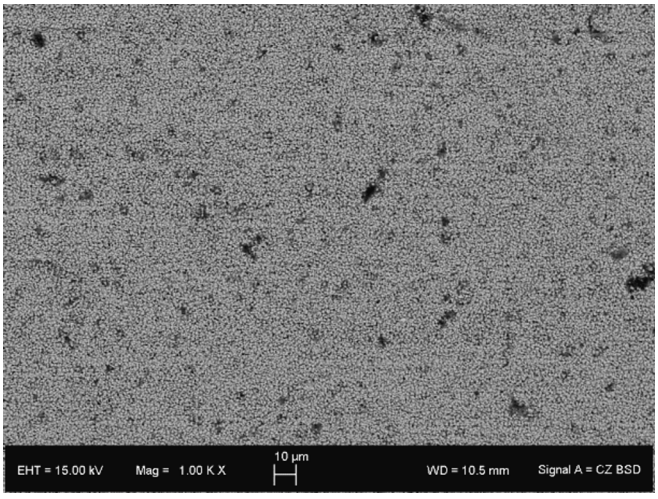


**Fig. 11.** Test 6 in surface view.

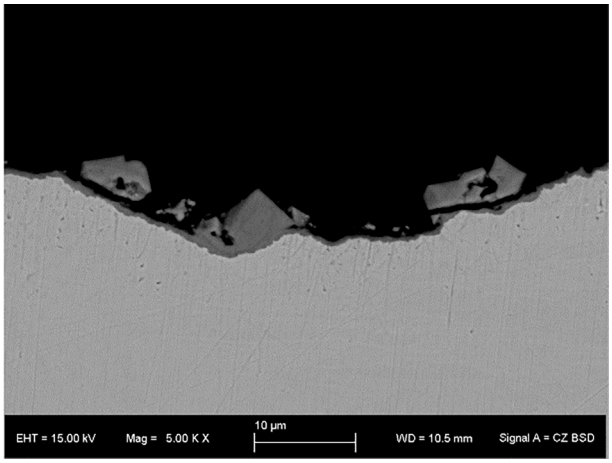


**Fig. 12.** Test 7 in section view.

For the first specimen, 3D images of the pits, along with colored bars indicating pit depth, are depicted in Fig. 14 and Fig. 15. These visuals suggest that pit 2 (Fig. 15) is deeper than pit 1 (Fig. 14). Nonetheless, quantitative insights can be gleaned from Fig. 16 and Fig. 17, as well as from Fig. 18 and Fig. 19, via profile analysis of pit 1 and pit 2. The profile analysis of the characteristic dimensions of the two pits is detailed in Table 9.

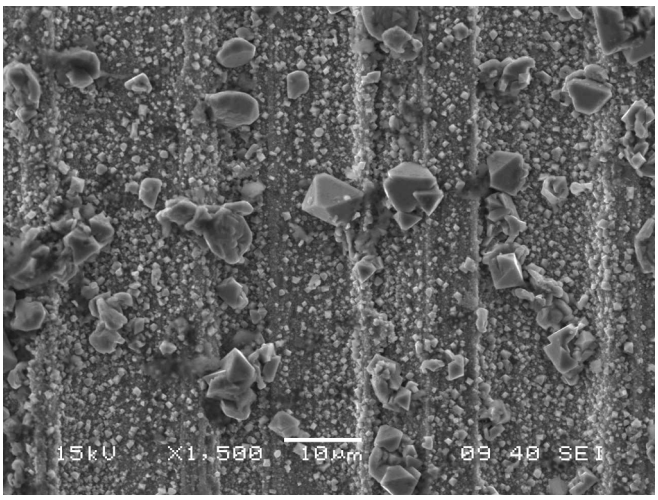


**Fig. 13.** Test 7 in surface view.

**Table 6**
Corrosion layer thickness.

| Test N. | Thickness [µm] |
|---|---|
| 3 | 1.24 ÷ 1.96 |
| 4 | 0.70 ÷ 1.06 |
| 5 | 0.560 ÷ 1.20 |
| 6 | 1.346 ÷ 2.078 |

**Table 7**
Adherent corrosion layer composition (wt %).

| Test N. | Composition (wt%) | | |
|---|---|---|---|
| | Fe | Cr | O |
| 3 | 86.28 | 1.48 | 11.67 |
| 4 | 72 | 14 | 12.6 |
| 5 | 68.8 | 19.8 | 13.8 |
| 6 | 66.8 | 18.11 | 14.06 |

**Table 8**
Not adherent corrosion layer composition (wt %).

| Test N. | Composition (wt%) | | |
|---|---|---|---|
| | Fe | Cr | O |
| 3 | 90.01 | 1.71 | 7.62 |
| 4 | 79 | 2 | 17 |
| 5 | 85 | 3.8 | 9.76 |
| 6 | 79.6 | 2.04 | 16.23 |

**Table 9**
Characteristics dimensions of pits.

| Pit n. | Max. Depth [µm] | Width [µm] |
|---|---|---|
| Pit 1 Specimen 1 | 18.5 | 26.6 |
| Pit 2 Specimen 1 | 23.3 | 27.5 |
| Pit 1 Specimen 2 | 28.2 | 18.2 |

From the second specimen, illustrated in Fig. 203D images of the pits are presented, accompanied by a colored bar offering qualitative and somewhat quantitative insights into pit depth. It is discernible that pit 1, situated on the left side, exhibits greater depth than pit 2, positioned on the right side. For these pits, quantitative data can be inferred from Fig. 21 and Fig. 22 through profile analysis of pit 1. The profile analysis of the characteristic dimensions of the two pits is delineated in Table 9.

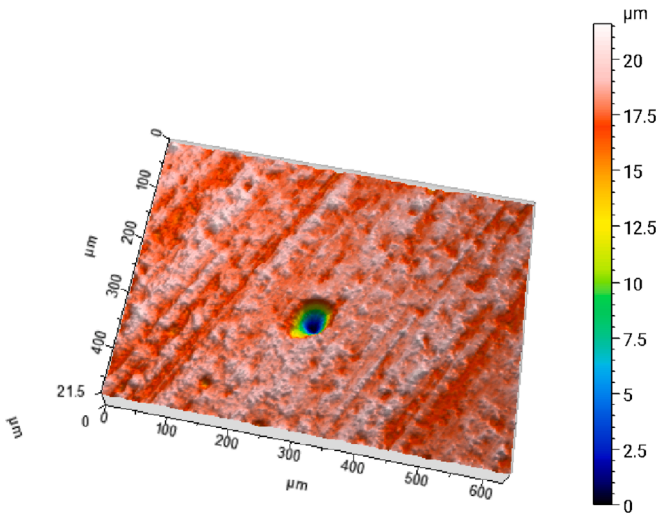


**Fig. 14.** 3D pit analysis – pit 1 of specimen 1.

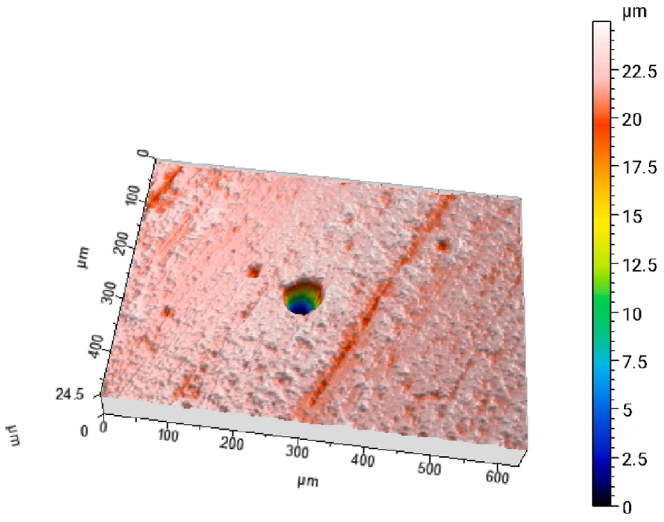


**Fig. 15.** 3D pit analysis – pit 2 of specimen 1.

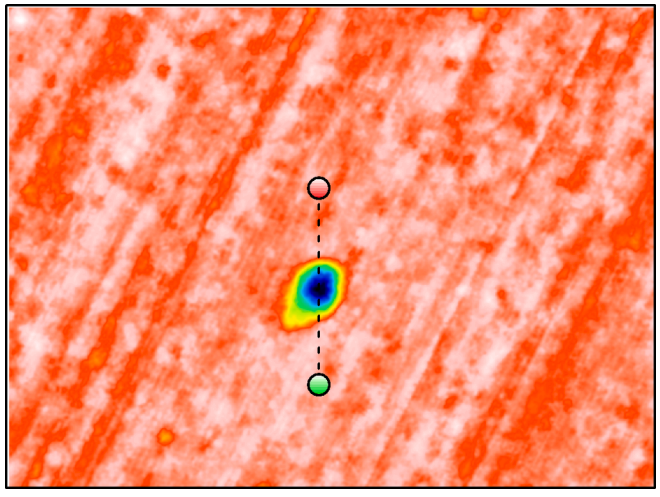

**Fig. 16.** 3D pit analysis – identification point for profile analysis (pit 1 of specimen 1).

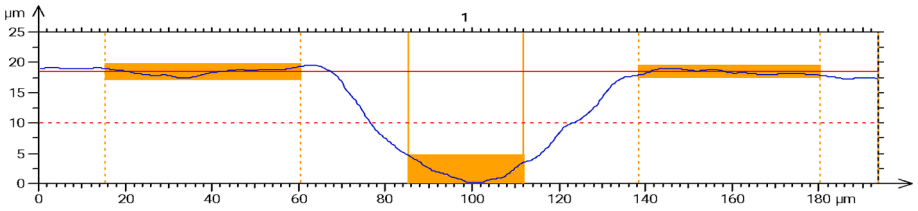


**Fig. 17.** 3D pit analysis – pit profile (pit 1 of specimen 1).

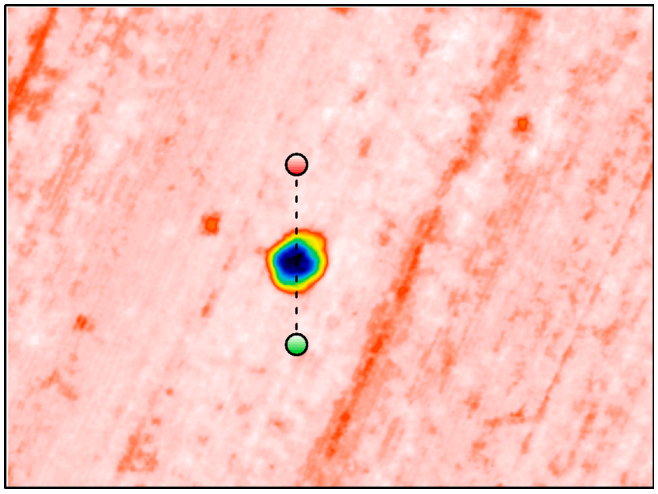

**Fig. 18.** 3D pit analysis – identification point for profile analysis (pit 2 specimen 1).

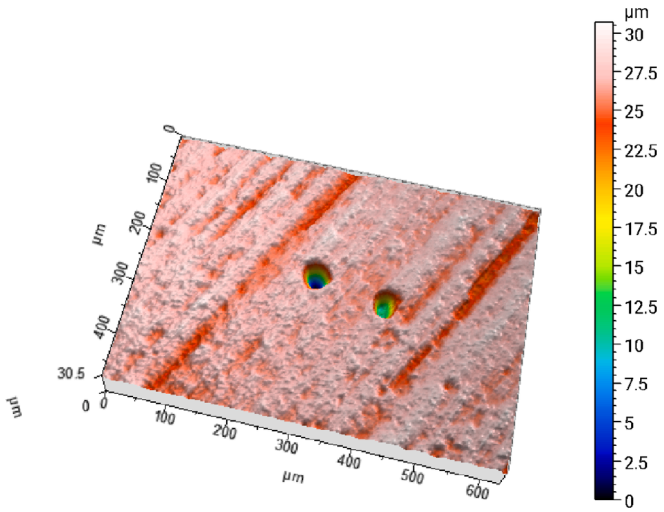


**Fig. 20.** 3D pit analysis – specimen 2.

Notably, only one profile analysis is conducted for this specimen due to the significant disparity in pit depth already depicted in Fig. 20.

## Discussion

The seven tests' results highlighted results that were in line with what was expected. Based on the chemical analysis results, there is an increase in KOH concentration until test 3. For the pH stability, it can be said that the aim has been achieved using a KOH concentration of 52 ppm. Indeed a pH between 9.0 and 9.5 entails a near-neutral pH when the fluid reaches 300 °C.

Considering what is reported in Table 4, it can be concluded that as the concentration of KOH increases, so does the release of Fe, Cr, Co, Mo, and W into the solution. However, the same trend is not observed for other species, as their correlation with KOH concentration does not show a consistent increase or decrease. Nevertheless, there is a general rise in Ni releases into the solution. Furthermore, with a stable KOH content and increasing oxygen concentration, there is a decrease in Fe release, coupled with an increase in W, Cu, and Co releases into the solution, despite the absence of a clear correlation between rising KOH concentration and increasing release. This variation in tendency, which starts from test 3, is correlated with the corrosion rate shown in Table 5.

About the experimented general corrosion, from Table 5, the

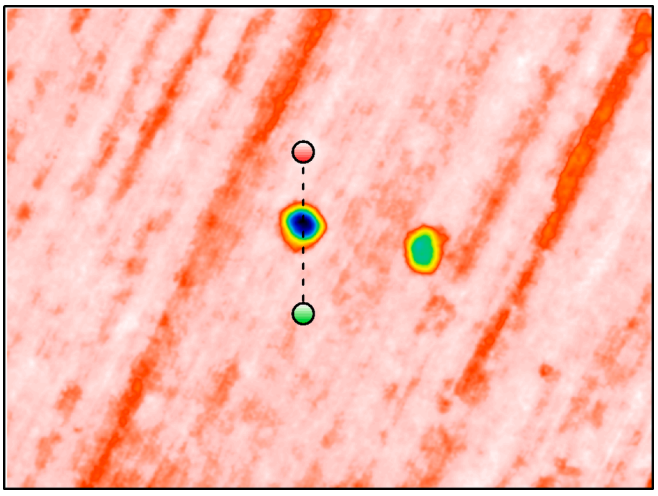

**Fig. 21.** 3D pit analysis – identification point for profile analysis (pit 1 specimen 2).

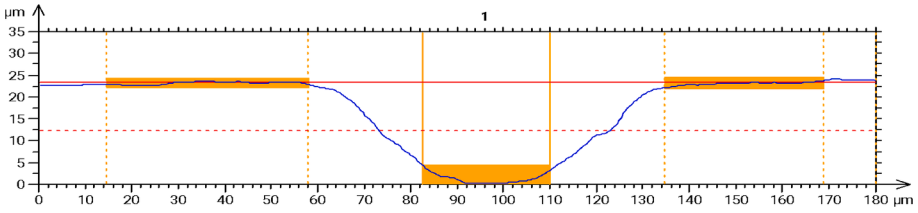


**Fig. 19.** 3D pit analysis – pit profile (pit 2 of specimen 1).

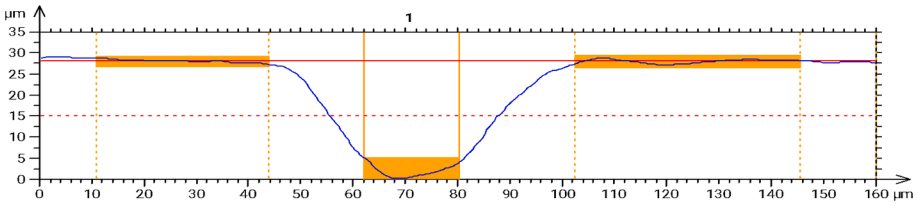


**Fig. 22.** 3D pit analysis – pit profile (pit 1 specimen 2).

corrosion rate follows an expected trend; thus, there is a decrease in corrosion rate until test 3 due to the increase in KOH concentration, so with a decrease in the pH stability of the solution. Moreover, from SEM analysis and EDS results, it has been observed and confirmed that the oxide scale comprises chromium-based and iron-based oxide in all specimens analyzed. Chromium oxide, known as chromite, constitutes the initial layer on the material surface. Conversely, iron oxide, termed magnetite, forms a secondary layer above the chromite layer, serving as protection for the non-stainless metal, particularly formed below 100 °C, as detailed in [16]. The distinction between the two layers is more discernible in Fig. 5 and Fig. 7, in the sectional view, and Fig. 10 and Fig. 11, in the surface view. It has to be noted that results from test 5 are similar to what can be obtained from a pickled specimen. This may have two different explanations: it is possible that before undergoing SEM and EDS analysis, the specimen has been pickled, or there is an effect coming from the procedure to prepare the specimen for the SEM and EDS analyses. The first explanation has been excluded, since the specimens follows a different path already from the collection time, at the autoclave opening. The second explanation is still being studied.

Moreover, outcomes from Table 7 need to be clarified. The cited results should be semi-quantitative since different effects could be considered when using an instrument such as SEM. Firstly, the electrons used with SEM are not in transmission; this means that the results come from a certain volume within the specimens. As a consequence, there is a limitation of the instrumentation because the oxide thickness values are close to the limiting operating range evaluable, which results in eventual contamination of the results by the composition of the base material matrix. From Table 7, it can be noted that it is mostly an enrichment of the adherent oxide layer in chromium.

From Table 6, an observation can be made regarding the effect of increasing oxygen concentration from test 3 to test 4, where a reduction in the disparity between maximum and minimum thickness is noted. Conversely, with a continued increase in oxygen concentration from test 4 to test 5, there is an escalation in this difference. Finally, in test 6, the difference between maximum and minimum thickness returns to the same value as observed in test 3. The last test presented in Table 6 reveals a thicker corrosion layer than the other two, suggesting that the pickling treatment of the specimens could be extended for a longer duration.

Doing a step foreword for localized corrosion phenomena, the aim pursued starting with test 3 has been achieved with test 7. Table 9 shows the characteristic dimensions of the four pits identified, and a comparison can be made between the different pits. From specimen 1, pit 2 seems the most alarming; however, comparing the results the pit 1 from specimen 2 is the deepest and the narrowest. This last configuration entails a potential material perforation in case of comparable dimensions between pit depth and material thickness. Pit propagation could be anticipated in experimental campaigns comprising longer tests than those outlined in Table 3.

In addition, the presence of pitting may be alarming because of the eventual superposition effect of Environmentally Assisting Cracking (EAC). A structural material exposed to an environment that enhances the effect of Stress Corrosion Cracking (SCC), Hydrogen Embrittlement (HC), or Liquid Metal Embrittlement (LME) may suffer from the presence of pitting corrosion because there can be a higher crack advance rate [18].

## Conclusions

The presented experimental study serves to scrutinize the corrosion dynamics of iron-based alloys within the confines of a FPP. Despite the limitations associated with the apparatus, such as the slight variation from the main thermal–hydraulic conditions, these investigations were meticulously tailored for applications in DEMO BB, driven by the imperative to curtail the generation of ACP, thereby mitigating its propagation within a cooling loop.

The exploration of water chemistry's influence on corrosion and release phenomena unfolded through two distinct analytical avenues. Firstly, meticulous efforts were made to uphold stable pH levels by continuous monitoring, not only at test onset and conclusion but also intermittently throughout the testing phase. Secondly, the quest to unearth localized corrosion phenomena involved augmenting oxygen concentrations in the water solution.

Fine-tuning the KOH concentration in the water solution aimed to establish a more consistent pH trend. However, heightened KOH levels engendered enhanced pH stability at the expense of heightened byproduct accumulation until test 3. This poses potential safety ramifications concerning radioactive contamination, necessitating strategic planning for decommissioning in a nuclear power plant's cooling circuit.

Tests, with and without pickling treatment, unveiled marked disparities in corrosion rates as KOH concentration surged to 52 ppm. Tests 1 and 2 evinced near-neutral pH levels at 25 °C, heating to 300 °C induced acidity. Hence, the 52 ppm KOH concentration was selected for oxygen control, premised on the alkaline pH observed at 25 °C in test 3.

Following the implementation of oxygen control, corrosion rates were reported in Table 5, illustrating a decline with escalating KOH concentration post-pickling treatment. This accords with expectations, given the typically positive correlation between acidity and corrosion rates.

Furthermore, oxygen control tried to identify a threshold above which localized phenomena manifest under specific environmental conditions. Test 7 revealed such occurrences when oxygen concentrations reached 400 ppb in the water solution, posing concerns over potential material piping perforation within a nuclear power plant's cooling circuit.

The investigations that were conducted encompassed a range of implications. Firstly, achieving consistent pH levels has allowed for a mitigation of the influence of water chemistry on the corrosion rate of alloys, particularly in terms of generalized corrosion. Furthermore, examinations into the critical oxygen concentration within the solution have revealed that beyond a specific threshold, an increased presence of ACPs associated with higher corrosion rates in specimens can be observed even after 1000 h of exposure. Although this scenario deviates significantly from the design conditions of the cooling loop, instances such as imperfect seals in connection systems (e.g., flanges) can facilitate the ingress of external ambient air into the piping, thereby promoting coolant oxygenation.

In localized corrosion cases, the material's structural integrity becomes a concern, as the re-passivation of the pitted surface is not an immediate outcome but a process contingent upon the chromium content within the material. EUROFER97, being in this study the alloy prone to pitting, contains chromium among its alloying constituents at levels below 10 % by weight, rendering it non-stainless and thus uncertain in

terms of re-passivation.

Failure to achieve re-passivation of the pipe material over extended periods exceeding 1000 h can lead to material cracking if the pit attains dimensions comparable to the pipe thickness. This eventuality would result in the loss of primary refrigerant, precipitating a Loss of Coolant Accident (LOCA), consequently allowing more air to infiltrate the circuit.

Future inquiries will delve into dissecting the impact of oxygen concentration on EUROFER alloy specimens graded by the EUROFusion consortium. These endeavors will leverage a larger HPHT loop apparatus equipped with mechanical stirring, obviating the need for a loop as stirring speeds of 5 m/s can be attained between specimens and the fluid. Additionally, investigations into pit propagation and re-passivation phenomena will ensue to address localized corrosion concerns.

## CRediT authorship contribution statement

**Martina Molinari:** Writing – review & editing, Writing – original draft, Methodology, Formal analysis, Conceptualization. **Eugenio Lo Piccolo:** Writing – review & editing, Writing – original draft, Methodology, Formal analysis, Conceptualization. **Raffaele Torella:** Writing – review & editing, Writing – original draft, Methodology, Formal analysis, Conceptualization. **Matteo D'Onorio:** Writing – review & editing, Supervision, Methodology, Conceptualization. **Nicholas Terranova:** Supervision, Methodology. **Gianfranco Caruso:** Supervision, Methodology, Formal analysis, Conceptualization.

## Declaration of competing interest

The authors declare that they have no known competing financial interests or personal relationships that could have appeared to influence the work reported in this paper.

## Acknowledgment

This work has been carried out within the framework of the EUROfusion Consortium, funded by the European Union via the Euratom Research and Training Programme (Grant Agreement No 101052200-EUROfusion). Views and opinions expressed are however those of the author(s) only and do not necessarily reflect those of the European Union or the European Commission. Neither the European Union nor the European Commission can be held responsible for them.

## Data availability

The data that has been used is confidential.

## References

[1] L. Di Pace, L. Quintinieri, Assesent of activated corrosion products for the DEMO WCLL, Fus. Eng. Des. 136 (2018) 1168–1172, https://doi.org/10.1016/j.fusengdes.2018.04.095.
[2] N. Terranova, Activation Corrosion Products (ACP) Assessment, Report IDM, EUROfusion, Garching, Germany, 2020.
[3] N. Terranova, ACPs Assessment for DEMO Divertor Cooling Loop, Report IDM, EUROfusion, Garching, Germany, 2022.
[4] International Atomic Energy Agency, Reactor Water Chemistry Relevant to Coolant-Cladding Interaction, IAEA-TECDOC-429, 1987.
[5] M.G. Fontana, Corrosion Engineering, Third Edition, McGraw-Hill Book Company, Singapore, 1987.
[6] K. Chen, M.R. Ickes, M.A. Burke, G.S. Was, The effect of potassium hydroxide primary water chemistry on the IASCC behavior of 304 stainless steel, J. Nucl. Mater. 558 (2002) 153323, https://doi.org/10.1016/j.jnucmat.2021.153323.
[7] E. Lo Piccolo, R. Torella, N. Terranova, L. Di Pace, C. Gasparrini, M. Dalla Palma, Preliminary assessment of cooling water chemistry for fusion power plants, Corr. Mater. Degrad. 2 (2021) 512–530, https://doi.org/10.3390/cmd2030027.
[8] C.A. Williams, E.A. Marquis, A. Cerezo, G.D.W. Smith, Nanoscale characterization of ODS-Eurofer 97 steel: an atom-probe tomography study, J. Nucl. Mater. 400 (2010) 37–45, https://doi.org/10.1016/j.jnucmat.2010.02.007.
[9] M. Klimenkov, R. Lindau, E. Materna-Morris, A. Moslanga, TEM characterization of precipitates in EUROFER 97, Prog. Nucl. Energ. 57 (2012) 8–13, https://doi.org/10.1016/j.pnucene.2011.10.006.
[10] S. Eshkabilov, I. Ara, I. Sevosianov, F. Azarami, X. Tangpong, Mechanical and thermal properties of stainless steel parts, manufactured by various technologies, in relation to their microstructure, Int. J. Eng. Sci. 159 (2021) 103398, https://doi.org/10.1016/j.ijengsci.2020.103398.
[11] A. Ouarga, T. Zirari, F. Simbarashe, M. Lahcini, H.B. Youcef, V. Trabadelo, Corrosion of iron and nickel based alloys in sulphuric acid: challenges and prevention strategies, J. Mater. Res. Technol. 26 (2023) 5105–5125, https://doi.org/10.1016/j.jmrt.2023.08.198.
[12] S. Rong, L. Huang, R. Wang, J. Xu, Z. Peng, Y. Chen, H. Jin, L. Guo, Corrosion behaviours of Ni-based and Fe-based alloys in supercritical water gasification with inorganic chloride salt, Corros. Sci. 219 (2023) 111241, https://doi.org/10.1016/j.corsci.2023.111241.
[13] T. Hernandez, P. Fernandez, Effect of the environment on the corrosion of EUROFER97 by solid lithium breeders, J. Nucl. Mater. 447 (2014) 160–165, https://doi.org/10.1016/j.jnucmat.2013.12.026.
[14] G. Shuwei, X. Donghai, W. Ning, W. Yuzhen, C. Gang, W. Shuzhong, Oxidation process and involved chemical reactions of corrosion-resistant alloys in supercritical water, Ind. Eng. Chem. Res. 59 (2020) 10278–10288, https://doi.org/10.1021/acs.iecr.0c01394.
[15] P. Arena, A. Del Nevo, F. Moro, S. Noce, R. Mozzillo, V. Imbriani, F. Giannetti, F. Edemetti, A. Froio, L. Savoldi, S. Siriano, A. Tassone, F.R. Urgorri, P.A. Di Maio, I. Catanzaro, G. Bongiovi, The DEMO water-cooled lead-lithium breeding blanket: design status at the end of the pre-conceptual design phase, Appl. Sci. 11 (24) (2021) 11592, https://doi.org/10.3390/app112411592.
[16] C. W. Turner, Formation of corrosion products of carbon steel under condenser operating conditions", paper presented at Nuclear Plant Chemistry Conference (NPC), Paris (France), 2012.
[17] M. Dunlap, J.E. Adaskaveg, Introduction to the Scanning Electron Microscope: Theory, Practice & Procedures, Presented by Facility for Advanced Instrumentation, U.C Davis, 1997.
[18] J.W. Martin, Materials for engineering, Third edition, Woodhead Publishing, England, 2006.